Available online at www.sciencedirect.com
ScienceDirect
Acta Materialia 56 (2008) 31–42
Acta MATERIALIA
www.elsevier.com/locate/actamat

On the origin of deformation-induced rotation patterns below nanoindents

N. Zaafarani, D. Raabe *, F. Roters, S. Zaefferer

Department of Microstructure Physics and Metal Forming, Max-Planck-Institut für Eisenforschung, Max-Planck-Straße 1, 40237 Düsseldorf, Germany

Received 22 June 2007; received in revised form 30 August 2007; accepted 1 September 2007
Available online 18 October 2007

Abstract

This study is about the origin of systematic deformation-induced crystallographic orientation patterns around nanoindents (here of single crystalline copper; conical indenter) using the following approach: first, the rotation pattern is investigated in three-dimensions (3D) using a high-resolution 3D electron backscattered diffraction (EBSD) technique (EBSD tomography) which works by a serial sectioning and EBSD mapping procedure in a scanning electron microscopy-focused ion beam cross-beam set-up. Second, the problem is modeled using a crystal plasticity finite element method which is based on a dislocation density-based constitutive model. Third, the results were discussed in terms of a geometrical model which simplifies the boundary conditions during indentation in terms of a compressive state normal to the local tangent of the indent shape. This simplification helps to identify the dominant slip systems and the resulting lattice rotations, thereby allowing us to reveal the basic mechanism of the formation of the rotation patterns. The finite element simulations also predict the pile-up patterning around the indents, which can be related to the dislocation density evolution.

Keywords: Nanoindentation; 3D EBSD; Crystal plasticity; Gradient; Geometrically necessary dislocations

1. Introduction

The observation of deformation-induced crystallographic lattice rotations caused by nanoindentation has recently attracted attention [1–8]. These orientation patterns were observed experimentally [1–4,7] and also in corresponding simulations [4,6]. Concerning the experimental work, it is important that the same rotation patterns were identified by using three different types of techniques performed by different groups, namely, synchrotron wide-angle Bragg diffraction [1], electron backscattered diffraction (EBSD) in two [7] and three dimensions [4], and transmission electron microscopy (TEM) [2,3]. The viscoplastic crystal plasticity finite element simulations which we published recently [4] could also capture some important features of the experimentally observed orientation patterns. However, irrespective of some success along this line, we must also state that a detailed simulation does not necessarily replace a firm understanding of the main mechanism which is responsible for the fact that such patterns exist at all. In other words, although good agreement was obtained in a previous experimental and theoretical study of this phenomenon [4], it remains unclear why these deformation-induced patterns consist of multiple narrow zones of alternating crystalline rotations and counter-rotations of equal magnitude in close sequence. In this paper, we therefore try to elucidate the general crystallographic principle behind these patterns. For this purpose, we take the following approach: first, the rotation patterns are investigated by a high-resolution three-dimensional (3D) EBSD technique (EBSD tomography) for a nanoindent performed by a conical indenter with a spherical tip in a copper single crystal. Next, we conduct advanced crystal plasticity finite element simulations which are based not on a viscoplastic formulation but on a dislocation density-based constitutive model [9,10]. Finally, the results are discussed in terms of a geometrical model which simplifies the boundary

* Corresponding author. Tel.: +49 211 6792 333.
E-mail address: d.raabe@mpie.de (D. Raabe).

1359-6454/$30.00
doi:10.1016/j.actamat.2007.09.001

conditions imposed during indentation in terms of a compressive state normal to the local tangent of the indent rim. This simplified assumption allows one to identify the dominant slip systems and the crystallographic principle behind the resulting reorientations. The finite element simulations also predict the pile-up patterning around the indents which can be related to the dislocation density evolution.

2. Modeling and simulation

2.1. Motivation

The deformation and reorientation patterns caused by nanoindentation motivate the use of a crystal plasticity finite element approach for obtaining a better understanding of this phenomenon. The crystal plasticity finite element method allows one to study the activation of certain slip systems at different stages of indentation, the change of the crystal orientation, and the formation of pile-up or sink-in patterns around the indent [11]. The strength of the method lies particularly in properly mapping the strong kinematical influence of crystalline anisotropy during plastic straining, which as a rule also leads to the prediction of the correct tendency in the resulting orientation changes. This has been shown in a number of studies [4,11–16] where predictions obtained by the crystal plasticity finite element method were compared in detail with corresponding micromechanical experiments with respect to strain, texture and forces. Conventional crystal plasticity models (e.g. [17,18]) use viscoplastic hardening laws as a good compromise between computation speed and predictive reliability. The shortcoming of such viscoplastic formulations is the absence of an internal variable concept beyond the incorporation of the crystal orientation. More advanced variants of the crystal plasticity finite element method, therefore, replace the viscoplastic constitutive description by dislocation-based models [9,10,19–26]. Since it is likely that some dislocation effects which cannot be readily captured by viscoplastic hardening laws may play a substantial role in nanoindentation of single crystals, we use in this study an advanced crystal plasticity finite element method which is based on dislocation rate formulations for the simulation of nanoindentation.

2.2. A physically based crystal plasticity model

2.2.1. Theory

The model which was introduced in Refs. [9,10] adopts the Orowan equation as a kinematic equation on each slip system to establish a connection between the shear rate and the mobile dislocation density

$$\dot{\gamma}_\alpha = \rho_{M\alpha} b v_\alpha \tag{1}$$

where $\dot{\gamma}_\alpha$ is the shear rate on slip system α and b is the magnitude of the Burgers vector. The mobile dislocation density, $\rho_{M\alpha}$, and the velocity of the dislocations, v_α, on a slip system α are treated as functions of the statistically stored dislocation density, ρ_{SSD}. In Ref. [9] it is shown that the mobile dislocation density can be approximated by

$$\rho_{M\alpha} = \frac{2k_B T}{c_1 c_2 c_3 G b^3} \sqrt{\rho_{F\alpha}} \sqrt{\rho_{P\alpha}} \tag{2}$$

where c_1, c_2 and c_3 are material constants, k_B is the Boltzmann constant, T is the absolute temperature and G is the shear modulus. The quantities $\rho_{F\alpha}$ and $\rho_{P\alpha}$ denote the forest dislocation density and the density of parallel dislocations, respectively. Both measures are calculated as projections of the statistically stored dislocation density ρ_{SSD} on the slip system α. Based on the cutting process of the forest dislocations, the average dislocation velocity can be calculated as

$$v_\alpha = \lambda_\alpha \nu_0 \exp\left(-\frac{Q_{cut} - (|\tau_\alpha| - \tau_{pass,\alpha}) V_\alpha}{k_B T}\right) \tag{3}$$

where

$$\tau_{pass,\alpha} = c_1 G b \sqrt{\rho_{P\alpha}} \tag{4}$$

is the shear stress required to move a dislocation past the other parallel dislocations.

$$\lambda_\alpha = c_2 / \sqrt{\rho_{F\alpha}} \tag{5}$$

is the jump width of the mobile dislocations related to the density of forest dislocations $\rho_{F\alpha}$.

The activation volume, V_α, resulting from the steps (kinks) created by the cutting process can be expressed as

$$V_\alpha = c_3 b^2 \lambda_\alpha \tag{6}$$

The quantities ν_0 and Q_{cut} in Eq. (3) are the attack frequency and the activation energy for the forest cutting process, respectively.

The evolution of the statistically stored dislocation density describes the hardening on each slip plane. The evolution Eq. (7) includes multiplication ($\dot{\rho}^+$) and annihilation ($\dot{\rho}^-$) terms for the statistical density of dislocations, ρ_{SSD}, in the form of a rate formulation,

$$\dot{\rho}_{SSD} = \dot{\rho}^{+1} + \dot{\rho}^{+2} - \dot{\rho}^{-1} - \dot{\rho}^{-2} \tag{7}$$

where $\dot{\rho}^{+1}$ and $\dot{\rho}^{+2}$ are the production rates of ρ_{SSD} due to the interaction with forest dislocations and dipole formation, respectively.

$$\dot{\rho}^{+1} = \frac{c_4}{b} \frac{1}{\lambda_\alpha} \dot{\gamma}_\alpha \tag{8}$$

$$\dot{\rho}^{+2} = \frac{c_5}{b} d_{dipole} \rho_M \dot{\gamma}_\alpha \tag{9}$$

c_4 and c_5 are fitting parameters,

$$d_{dipole} = \frac{Gb\sqrt{3}}{16\pi(1-\nu)(|\tau_\alpha| - \tau_{pass,\alpha})} \tag{10}$$

is the critical distance for dipole formation [24] and ν is the Poisson's ratio. The rates $\dot{\rho}^{-1}$ and $\dot{\rho}^{-2}$ are the non-thermal and thermal annihilation rates of the dislocations, respectively.

$$\dot{\rho}^{-1} = c_6 \rho_{SSD} \dot{\gamma}_\alpha \tag{11}$$

$$\dot{\rho}^{-2} = c_7 b \rho_{SSD}^2 \frac{D_{df} A_{ac} b^2}{k_B T} \tau_\alpha \exp\left(-\frac{Q_{bulk}}{k_B T}\right) \dot{\gamma}_\alpha^{c_8} \tag{12}$$

where c_6 and c_7 are fitting parameters, D_{df} is the pre-exponential part of the diffusion coefficient, A_{ac} is the activation area and Q_{bulk} is the activation energy for self diffusion. As the deformation takes place at room temperature, the thermal annihilation term, Eq. (12), was neglected.

2.2.2. Parameter sensitivity and fitting procedure

The evolution equations involve a number of material parameters (c_1–c_6) which have to be fitted using experimental data. For the determination of the proper values of the material parameters, a compression test was performed on a copper single crystal. The shape of the compression sample was a cylinder with dimensions 3 mm × 4.5 mm. The compression speed was 0.1 mm s^{-1}, resulting in an average overall strain rate of 4.3×10^{-4} s^{-1}. As the compression axis was in the [1 1 1] crystal direction, no rotation was expected ([1 1 1] is stable under compression). Due to the high symmetry of this orientation, the deformation is achieved by the activation of at least six slip systems. A shear stress–shear strain curve for a single slip system was extracted from the experiments by using the appropriate Schmid factor and comparing it with the corresponding curve calculated analytically from the evolution equations. Fig. 1 illustrates the very good agreement between the model and the experiment. Table 1 comprises the fitted parameters and the main constants. All parameters except the initial dislocation density are dimensionless. The activation energy for the slip of edge dislocations, Q_{cut}, was approximated by $\frac{1}{2}Gb^3$, which results in a value of 6.33×10^{-19} J for Cu. The attack frequency of a dislocation segment is fixed to a constant value of 10^{10} s^{-1} according to Ref. [27].

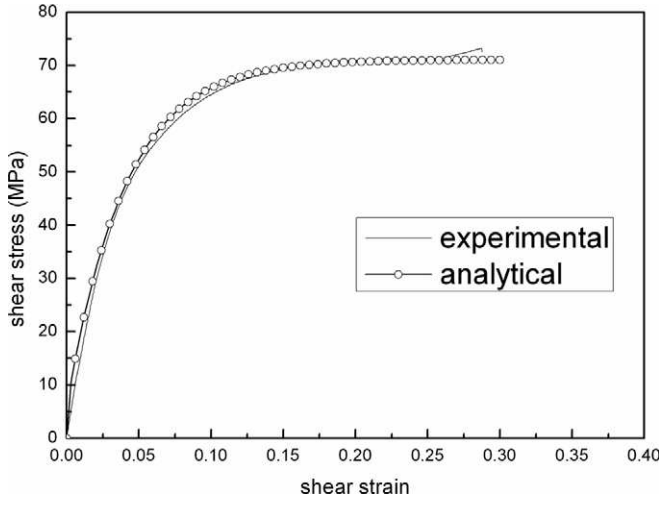

Fig. 1. Fitted shear stress–shear strain curve: (a) undeformed mesh and (b) mesh after indentation

However, as the scale of the two experiments (compression, nanoindentation) differs in size, the fitted values may also be different for the two scales. This applies in the current case for the value of the initial dislocation density. Although the original single crystal fit procedure provided a value of 5×10^{10} m^{-2}, a higher value of 10^{12} m^{-2} was chosen in the actual simulations since the simulated force–depth curves in this case revealed a better match when compared with the ones observed in the nanoindentation experiments. Even though this seems like a large discrepancy, it can be understood by local deviations from the average dislocation density and also the rapid increase of the dislocation density at the very beginning of plastic deformation.

At first sight, the dislocation-based model uses a similar number of fit parameters as empirical models. However, it must be emphasized that a major advantage of the dislocation-based model is that all parameters have a physical meaning and that they can be further coupled to metallurgical mechanisms and multiscale models. All parameters that were used lie within the range expected according to Ref. [9].

2.3. Details of the crystal plasticity finite element model implementation

The finite element code MARC was used as a solver for the constitutive model discussed above via the user-defined subroutine HYPELA2 [28]. The mesh consisted of 4312 elements and 5224 nodes (Fig. 2a). The elements were of the 3D hexahedral type, with eight integration points. Near the center of the indented area a finer mesh was used due to the high deformation gradients expected in this zone (Fig. 2b). The lower face of the cylinder was fixed. Otherwise, each node possessed three translational and three rotational degrees of freedom. The kinematics were based on an updated Lagrangian scheme.

The tip with a radius of 1.5 μm was modeled as a rigid body. The simulation was performed with displacement control up to an indentation depth of 1 μm in the negative [1 1 1] crystallographic direction. The initial orientation of the single crystal sample was chosen by selecting appropriate Euler angles (0, 54.74 and 45°, Bunge's notation) such that the x, y, z coordinate system represented the $[1\,\bar{1}\,0]$, $[1\,1\,\bar{2}]$ and [1 1 1] crystal directions, respectively (Fig. 4).

3. Experimental procedure

Nanoindents were conducted using different forces on a Cu single crystal with a Hysitron nanoindenter system (TriboIndenter). The largest indent was 1 μm deep. The force direction was in the negative [1 1 1] direction of the crystal. The tip had a conical shape with a spherical tip in order to avoid any symmetry in the experiment other than that of the crystal. A scanning electron microscopy (SEM) image of the used indenter tip is illustrated in Fig. 3. The EBSD experiments were conducted by using a

Table 1
Summary of crystal constants and parameters used in the model

Material constant	Unit	Value	Parameter	Unit	Value
Shear modulus, G	GPa	75.4	For passing stress, c_1	–	0.1
Burgers vector, b	m	2.56×10^{-10}	For jump width, c_2	–	1.95
Attacking frequency, v_0	s^{-1}	10^{10}	For obstacle width, c_3	–	0.3
Activation energy of slip, Q_{cut}	J	6.33×10^{-19}	For lock formation, c_4	–	0.037
Poisson's ratio, v	–	0.33	For dipole formation, c_5	–	0.04
			For athermal annihilation, c_6	–	50
			Initial dislocation density, ρ_0	m^{-2}	5×10^{10}

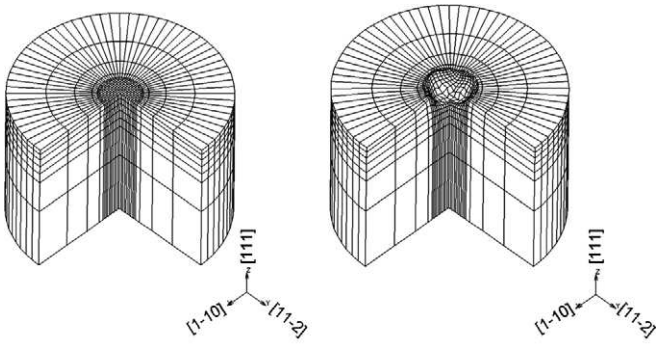

Fig. 2. The mesh used in finite element simulation (one quarter of the mesh is not shown).

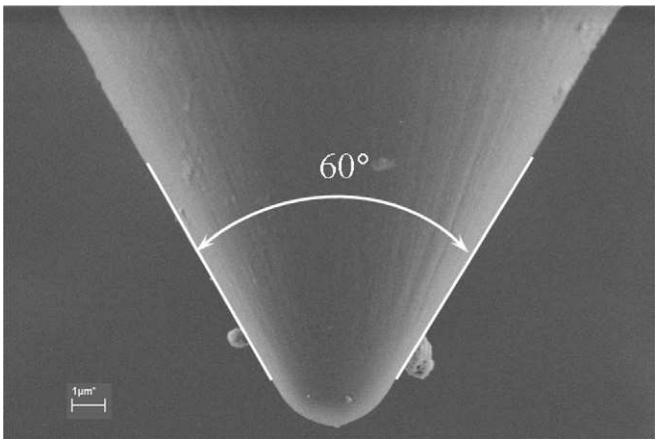

Fig. 3. SEM image of the used diamond indenter tip.

joint high-resolution field emission SEM–EBSD set-up together with a focused ion beam (FIB) system in the form of a cross-beam 3D crystal orientation microscope (3D EBSD). Details of this novel experimental approach are given in Refs. [4,29]. The FIB was directed normal to the (1 1 1) plane, producing successive parallel milled areas, as illustrated in Fig. 4. After each milling step an EBSD map was taken (Fig. 5). By the alternating milling and EBSD steps a tomographic 3D EBSD image of the spatial crystal misorientation distribution underneath the nanoindent was reconstructed. Further details on the indentation procedure are given in Refs. [4,11].

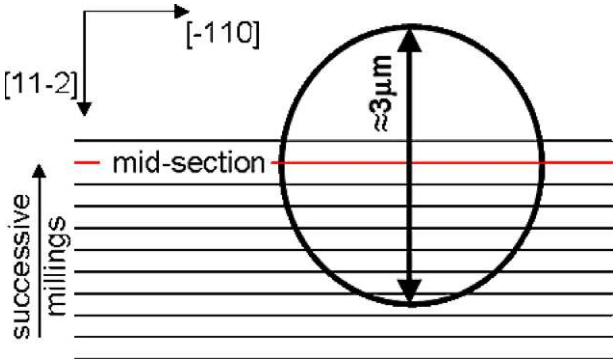

Fig. 4. Top view presenting the cutting planes relative to the indent position.

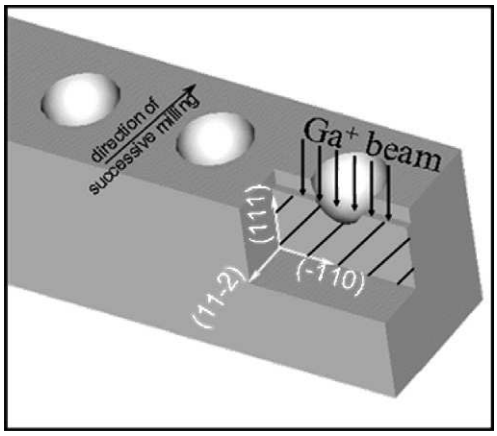

Fig. 5. Schematic drawing of the successive section milling and EBSD measurement.

4. Comparison between experimental results and the dislocation-based crystal plasticity finite element model

4.1. Rotation patterns in crystal misorientation presentation

The set of successive sections shown in Fig. 6 compares the misorientation values for the crystal in the measured $(1\,1\,\bar{2})$ serial sections (Fig. 6a1–a4) with the simulations (Fig. 6b1–b4). All sections shown are near the indent center. The large accumulated strains in this region allow a more detailed study of the misorientation changes. The color code indicates the magnitude of the orientation changes relative to the initial undeformed crystal orientation.

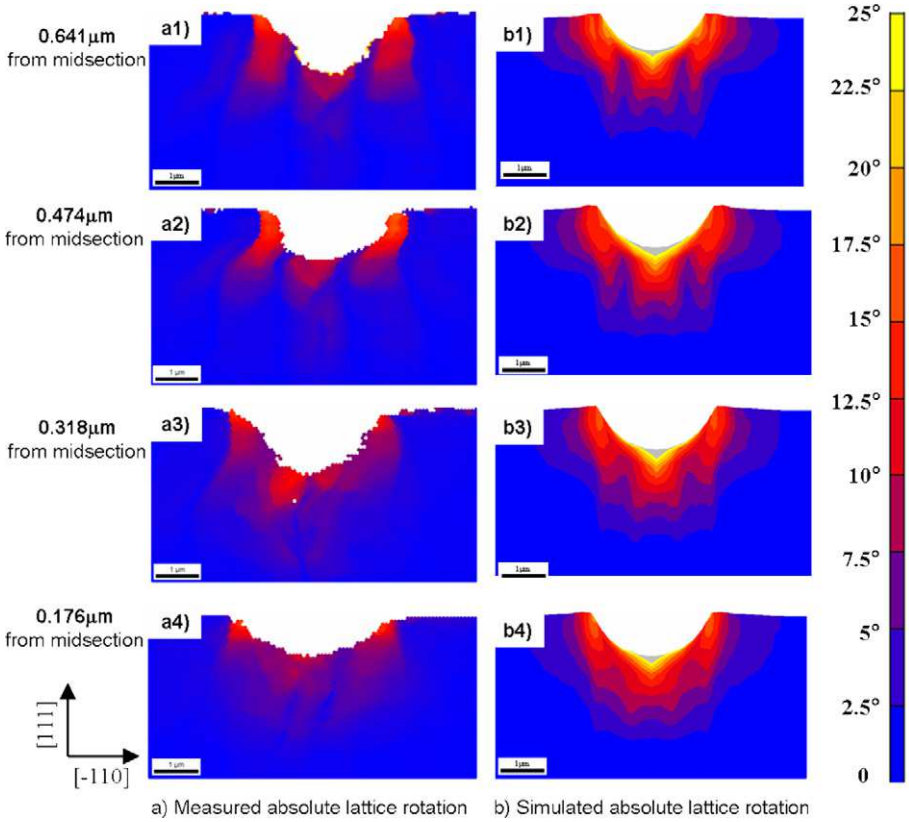

Fig. 6. Misorientation maps (absolute lattice rotation) underneath the indentation at different cross sections, comparison between experimental and simulation results. (The seemingly shallower indent near the center is due to the edge effects and milling-induced curvature.)

The measurements reveal a pronounced deformation-induced crystal rotation pattern underneath the indent, as reported previously [4]. The alternating rotation and reorientation zones are arranged directly underneath the indent. The measurements show that at the sides of the nanoindent only very small crystallographic rotations took place. The pattern underneath the indent near the center section can be characterized by six rotation zones which are separated by narrow rotation-free areas (Fig. 6a4). The maximum values of the misorientation angles can be observed at the surface directly at the contact layer.

4.2. Rotation patterns in axis-angle presentation

The orientation maps are also represented in the form of rotation angles about the $[1\,1\,\bar{2}]$ crystal direction in the sample reference system (note that in Ref. [4] the axis rotation is given in the crystal coordinate system). The maps are plotted on the $(1\,1\,\bar{2})$ planes in Fig. 7a1–a4 at different spacing to the center of the indent. The maps reveal pronounced lattice rotations about the $[1\,1\,\bar{2}]$ axis below the indent and lower values at the rims of the indent. The measurements also show frequent and quite abrupt changes in the sign of the rotation direction along and near the surface when presented in the form of $[1\,1\,\bar{2}]$ axis rotations. The rotations decrease further away from the contact zone. The comparison with the dislocation-based crystal plasticity finite element model shows that it succeeded in capturing fine details of the crystallography of the rotation patterning (Fig. 7b1–b4). Concerning the absolute values of the rotation angles about the $[1\,1\,\bar{2}]$ axis, a maximum rotation angle of 14° was observed in the experiment. The corresponding maximum in the dislocation-based crystal plasticity model is about 23°. This deviation could be due to edge effects at the contact zone and milling-induced curvature caused by the ion beam so that no complete EBSD mapping could be made up to the actual contact interface. In this region, though, maximum rotation values are likely to occur. Also, the lateral resolution of the measurement which was conducted using a 80 nm step size was probably not fine enough to capture all the effects at the actual contact surface.

4.3. Pile-up pattern formation around the indent

The pile-up pattern surrounding the $[\bar{1}\,\bar{1}\,1]$ indent is characterized by a sixfold symmetry, as already reported by Wang et al. [11]. The simulations reveal the same pattern (Fig. 8). Comparing the pattern of the mobile dislocation density around the indent (Fig. 9) with the pile-up reveals some common features. The mobile dislocations are arranged around the indent in a pattern similar to the pile-up distribution. In fact, the peak values for the mobile dislocation density are found in almost the same positions

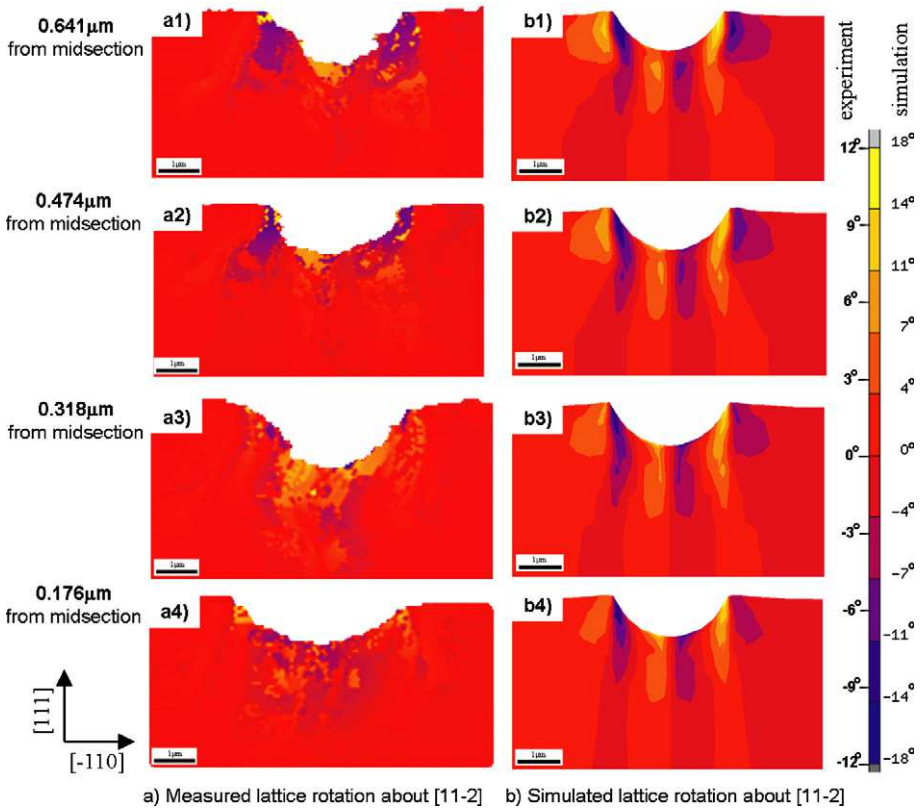

Fig. 7. Comparison between crystal rotation about the direction $[1\,1\,\overline{2}]$ in the sample reference system underneath the indentation at different cross sections between experimental and simulation results (positive values mean counter clockwise rotation). Note that in [4] the axis rotation is given in the crystal coordinate system.

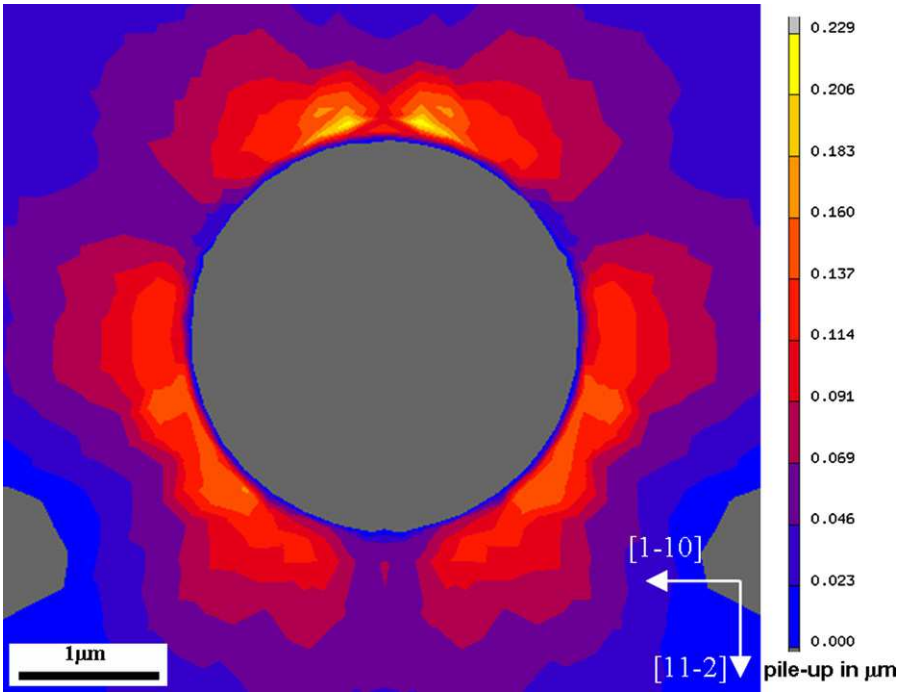

Fig. 8. Pile-up pattern around the nanoindent.

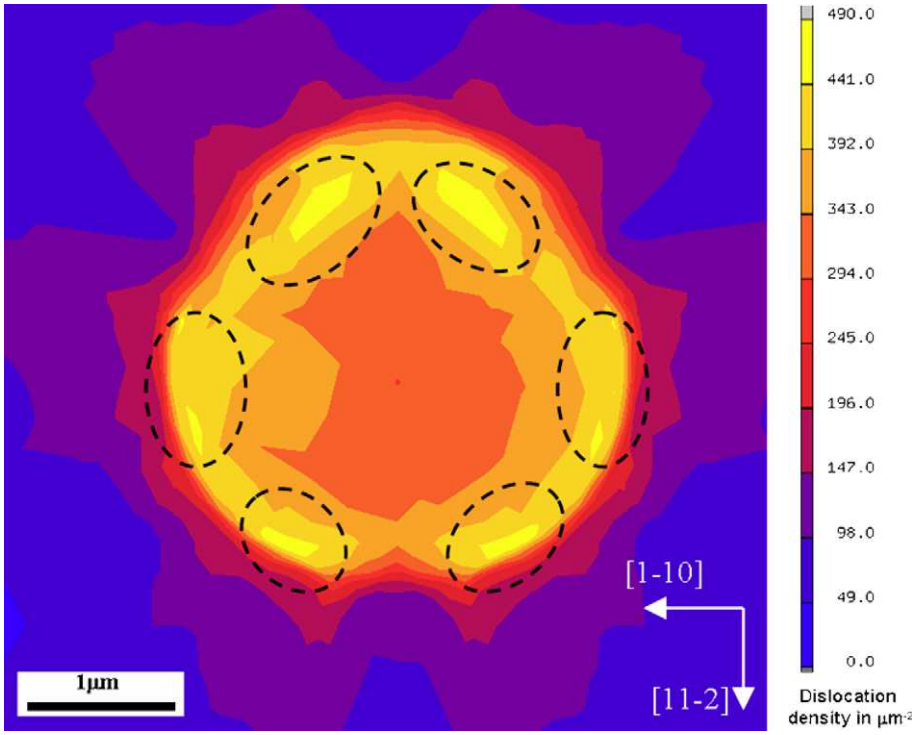

Fig. 9. Distribution of the mobile dislocation density close to the surface.

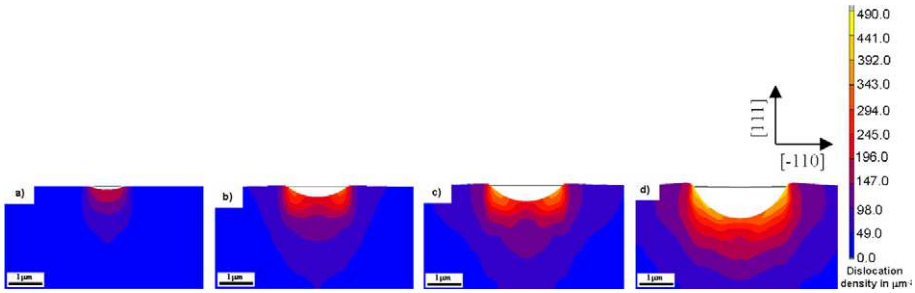

Fig. 10. Development of mobile dislocation density around the indent on a $\{1\,1\,\bar{2}\}$ midsection at: (a) 10% indentation (0.1 μm depth) (b) 30% indentation (0.3 μm depth) (c) 50% indentation (0.5 μm depth) and (d) 100% indentation (1 μm depth).

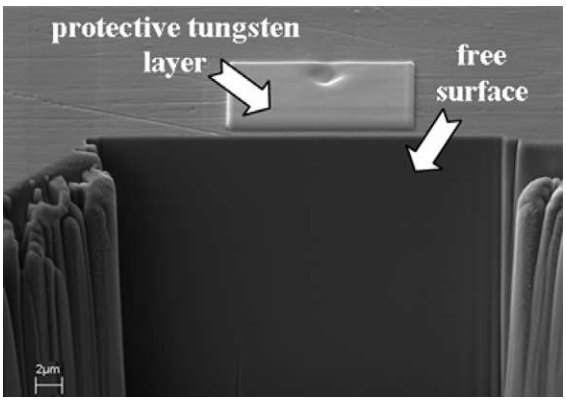

Fig. 11. SEM image of a serial section: (a) non-relaxed and (b) relaxed.

as the maximum pile-ups. This observation reflects the obvious connection between the local shear and the activity of the mobile dislocations.

Fig. 10 shows the evolution of the mobile dislocation density, ρ_M around the indent on a $\{1\,1\,\bar{2}\}$ midsection. In the first phase of the indentation the dislocation density shows a local peak directly underneath the indenter tip. As the indentation proceeds, the peak of the mobile dislocation density migrates towards the sides of the indent. As a consequence of this dislocation activity, the material flows along the path of least resistance. This tendency minimizes the strain energy and, since the contact area to the indenter acts as a rigid boundary, the most adequate path for the excess material is to flow towards the free surface, which leads to pile-ups.

4.4. Effect of the free surface

One drawback of the FIB technique for serial sectioning is that the method is destructive. This means that any error in the milling procedure requires full repetition of the entire

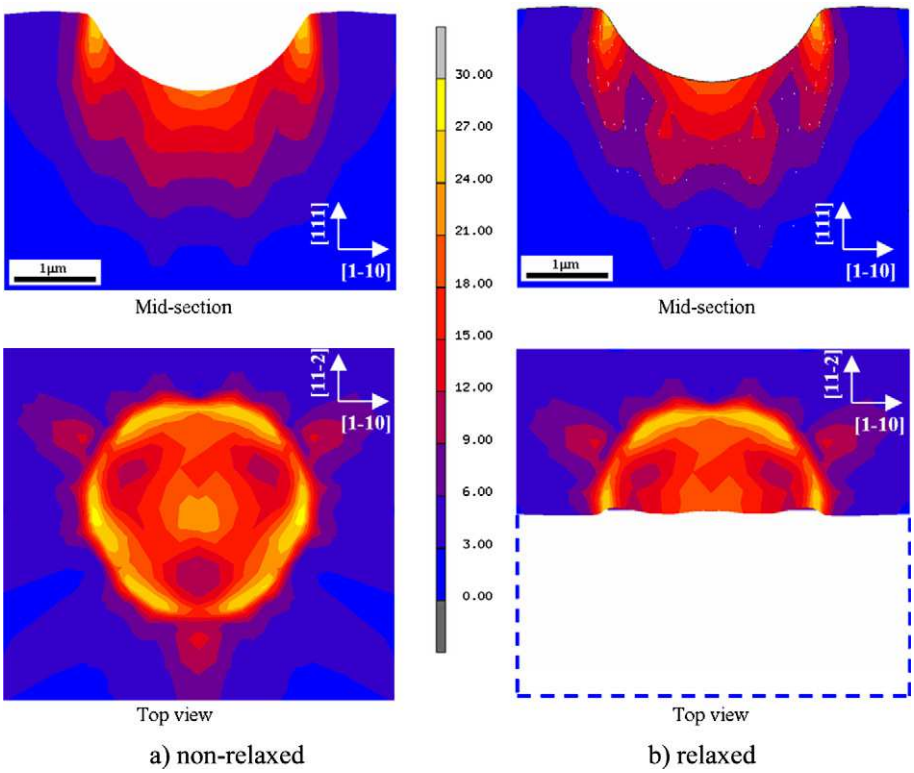

Fig. 12. Effect of free surface milling on the total crystal rotation at the center cross section.

experiment. Another problem of the method lies in the fact that the approach steadily produces new free surfaces for EBSD characterization (Fig. 11). This might have a small effect on the measured orientations compared with the (hypothetical) state of a bulk crystal without free surfaces.

With the help of the FE simulation, the error caused by the free surface can be estimated. For this purpose, the boundary conditions were changed to mimic a free surface (relaxed model). This approach simulates the effect of cutting the surface free. The misorientation patterns predicted in the two model variants are compared in Fig. 12. The comparison shows that, although the misorientation pattern remains almost unchanged, some deviations occur in the absolute values. The difference varies between 5 and 8% from the initial model (which is referred to here as the non-relaxed model variant).

5. Discussion

The phenomenon addressed in this paper is the gradual formation of systematic orientation patterns in the deformed zone underneath an indent caused by conical nanoindentation with a spherical tip. The patterns are particularly characterized by systematic arrangements of rotation and counter-rotation fields, as presented in the figures above. These rotation- and counter-rotation patterns were confirmed both by the measurements and by the simulations.

The first approach to better understand the rotation patterns is to conduct a detailed analysis of some selected nodes in the finite element analysis. On the surface of the sample along the $[1\,1\,\bar{2}]$ crystallographic direction the rotations about the $[1\,\bar{1}\,0]$ axis indicate the mentioned phenomenon, as shown in Fig. 13a. Three regions are inspected by selecting corresponding nodes (Figs. 13). Node (a) is chosen very close to the center, where the crystal reveals a negative rotation. While node (c) represents the neighboring positive rotation area, node (b) stands for the cross-over region between the two counter-rotated areas. This means that at node (b) almost no crystal rotation is expected to take place.

While Fig. 14 reveals the evolution of the rotation about the $[1\,\bar{1}\,0]$ direction (x-axis) during the indentation, Fig. 15 represents the corresponding slip system activity. It can be seen from Fig. 15a that close to the center the crystal undergoes a small positive rotation at the beginning of the indentation, which soon reverses its sense. Moving outwards from the center (Fig. 14b and c), the positive rotation increases until it dominates the whole indentation process. A likely interpretation of this observation is that the crystal rotation behavior is influenced by two different mechanisms. The first one is caused by the spatial rotations due to the geometry of the indenter. This means that certain rigid body rotations are imposed by the antisymmetric portion of the external displacement gradient tensor which is generated by the indentation process. The local crystallographic slip is responsible for the second kind of rotation.

In a second approach to better understand the reason for the rotation patterns we consider as a simple approximation the compression force exerted by the indenter as the only loading source. This force acts almost perpendic-

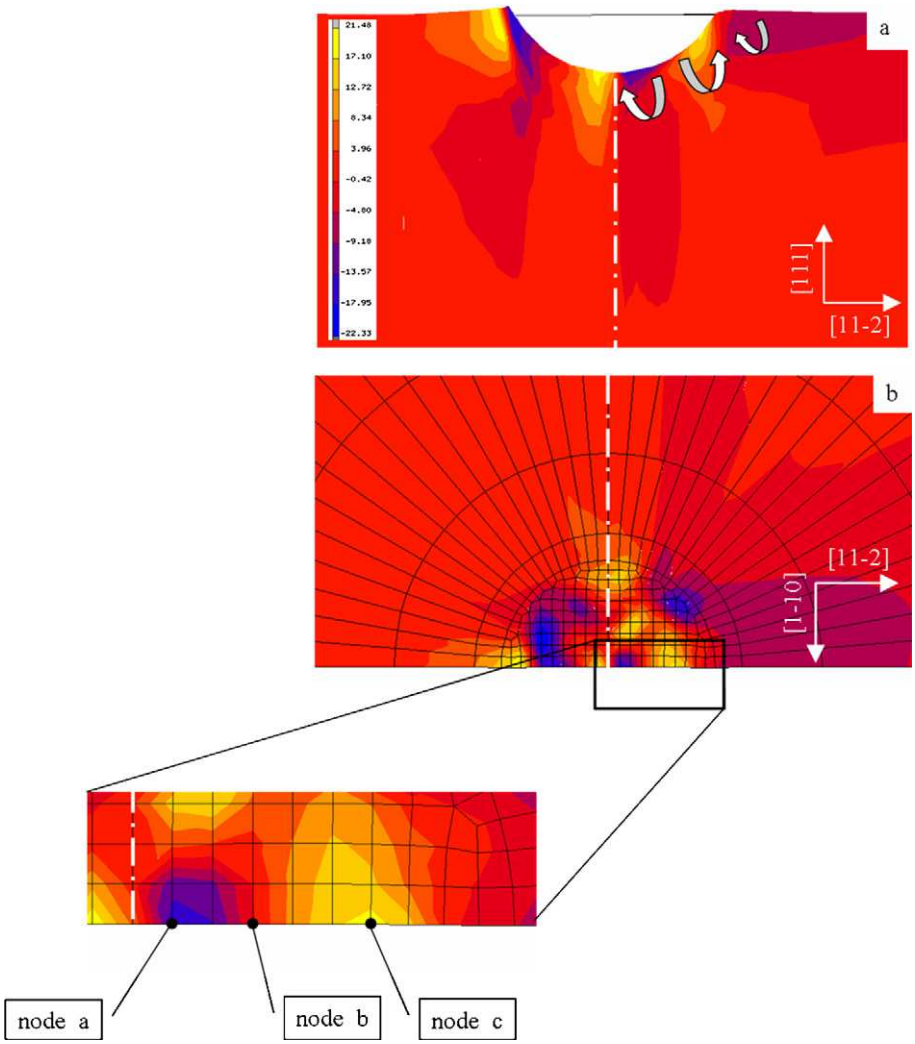

Fig. 13. Three nodes with different rotations on the $(1\bar{1}0)$ plane are chosen for investigation: (a) $[1\bar{1}0]$ rotations on a front view at the middle cross section and (b) Same rotations on the surface of the crystal.

ular to the local contact surface tangent between tool and crystal (schematical image in Fig. 16).

The components of the contact force at the selected nodes are extracted from the simulation results. Knowing the orientation of the crystal at each node allows the determination of the crystallographic direction of the loading axis during the whole indentation process.

This is shown in the schematical image on the right-hand side of Fig. 16, where a simplification is described which is used to track the changes in the single crystal kinematics during indentation in terms of a Sachs loading case under simple compression tangential to the local contact interface.

In the projection shown in Fig. 16 the corresponding evolution of the compression axis is plotted for the various nodes. For all nodes the compression axis lies on the $[00\bar{1}] - [\bar{1}\,\bar{1}\,\bar{1}]$ boundary. This is also expected due to the symmetry of the problem resulting in a rotation about the $[1\bar{1}0]$ axis. The movement of the compression axis along the $[00\bar{1}] - [\bar{1}\,\bar{1}\,\bar{1}]$ boundary results in simultaneous slip on pairs of two slip systems, as can be seen in Fig. 15. It can also be observed that at the beginning of the indentation process the axis rotates towards the $[\bar{1}\,\bar{1}\,\bar{1}]$ direction for all selected nodes ($1 \rightarrow 2$ in Fig. 16), before it reverses its motion towards the $[00\bar{1}]$ pole, ($2 \rightarrow 3$ in Fig. 16). This confirms the results of Fig. 14.

The question that arises is: why does the compression axis reverse its sense of rotation? The answer can be given by monitoring the slip systems involved in the process. At the beginning of the indentation three pairs of slip systems are activated, as indicated in Fig. 15. Slip system pair (1) consists of $[10\bar{1}](\bar{1}\,1\,\bar{1})$ and $[01\bar{1}](\bar{1}\,1\,\bar{1})$, pair (2) of $[\bar{1}0\bar{1}](1\,\bar{1}\,\bar{1})$ and $[0\bar{1}\,\bar{1}](\bar{1}\,1\,\bar{1})$ and pair (3) of $[\bar{1}\,\bar{1}0](1\,\bar{1}\,\bar{1})$ and $[\bar{1}\,\bar{1}0](\bar{1}\,1\,\bar{1})$. It is well known [30] that for a single crystal under compression the rotation of the compression axis towards the slip plane normal of the active slip system is the primary rotation. Therefore, and also from Figs. 16 and 17, one can see that the slip system pair (1) causes the compression axis to rotate towards the $[\bar{1}\,\bar{1}\,\bar{1}]$ pole following the reorientation route ($1 \rightarrow 2$), leading to an initial positive crystal rotation. However, this rotation reduces its Schmid factor and hence the shear activity is lowered, as can be seen in Fig. 15a.

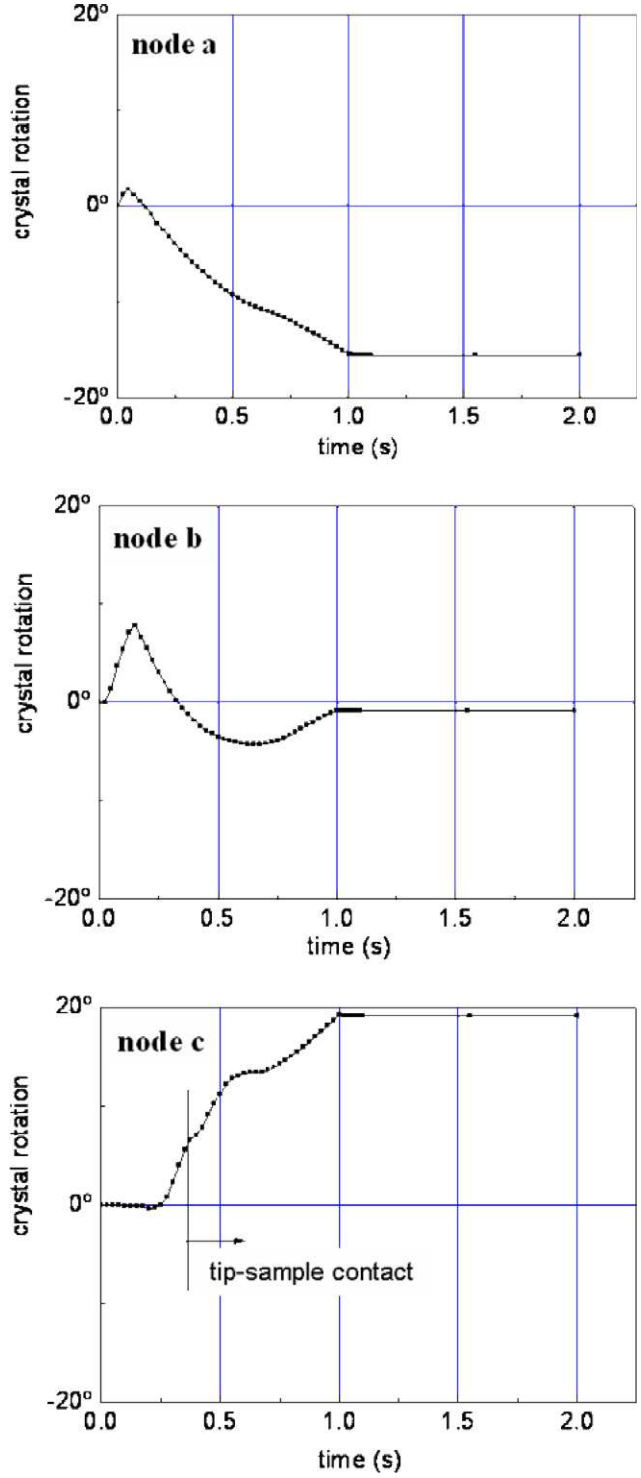

Fig. 14. The evolution of the total crystal rotation about $[1\bar{1}0]$ during indentation at: (a) node a, (b) node b and (c) node c.

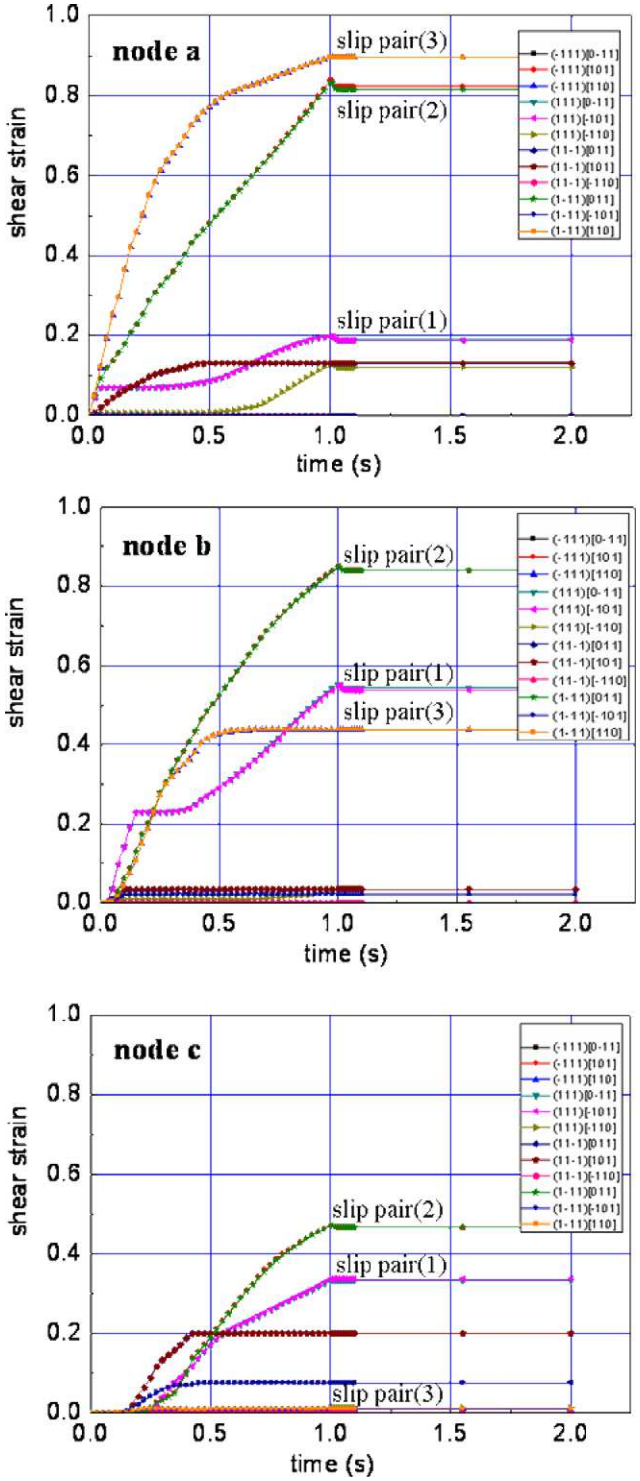

Fig. 15. The active slip systems during indentation at: (a) node a, (b) node b and (c) node c.

On the other hand, the two other slip system pairs (2) and (3) remain fully active with progressing indentation. Each pair tends to rotate the compression axis according to the route $(2 \rightarrow 3)$ (Fig. 16), towards the $[00\bar{1}]$ pole, which lies on the great circle going through the two slip plane normals of the pairs $(\bar{1}1\bar{1})$ and $(1\bar{1}\bar{1})$. Position (2) for node (a) (see Fig. 16) in Fig. 15a is located where the two rotation mechanisms equilibrate and the crystal reverses its sense of rotation. Route $(2 \rightarrow 3)$ describes a compression axis rotation in the positive direction around $[1\bar{1}0]$, i.e. a negative crystal rotation occurs.

The same slip mechanism occurs for node (b). The difference with respect to node (a) is caused by the tip geometry. By moving outward along the tip, the direction of the

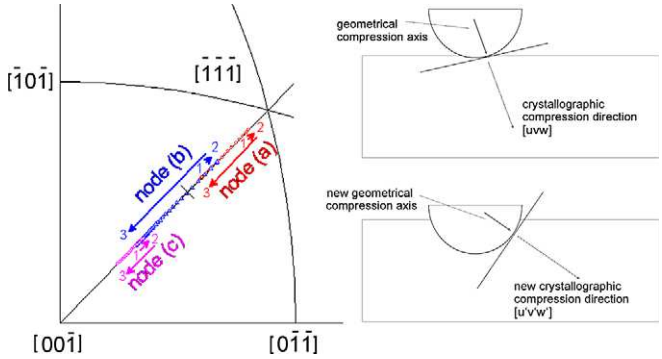

Fig. 16. Inverse pole figure revealing the rotation of the compression axis during indentation at the selected node positions a, b and c. The black cross represents the [11] direction. The schematical image on the right-hand side shows a simplification which describes the changes in the single crystal kinematics during indentation in terms of a Sachs loading case under simple compression tangential to the local contact interface.

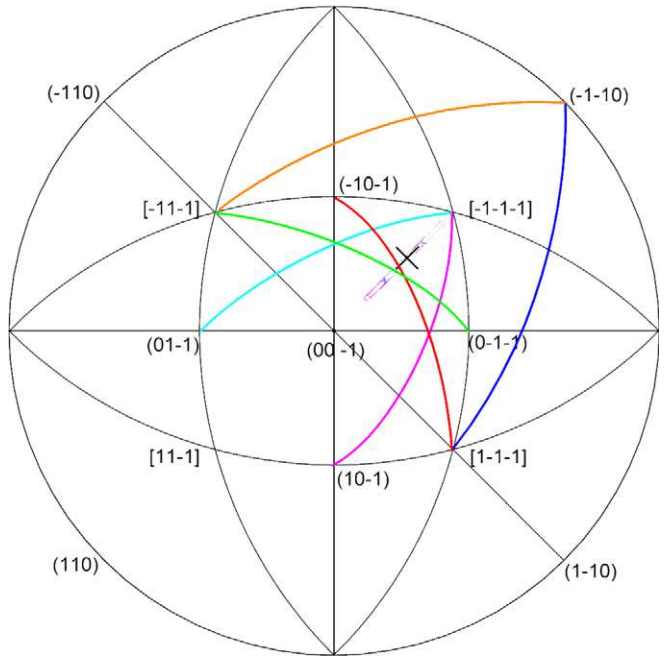

Fig. 17. The active slip systems in the indentation process with a conical indenter. The black cross represents the [11] direction. The curved lines connect the slip normal and slip direction of a specific slip system. See also magnification in Fig. 16.

compression axis moves away from the ($\bar{1}\bar{1}\bar{1}$) pole (Fig. 16). This results in a decreased slip activity of slip system pair (3) on the one hand and on the other hand extends the activity of the slip system pair (1). This explains the higher value of the initial positive lattice rotation illustrated in Fig. 14b compared with node (a) in Fig. 14a. At the end of the indentation the two opposite rotations compensate each other, resulting in an almost zero total rotation of the crystal. It is expected that by further indenting this position, the rotation-free zone will move outwards, further away from the center of the indent.

For node (c) the slip state is more complicated as the contact with the indenter tip occurs only after more than 35% of the indentation process. This means that other loading components also influence the initial rotations of the crystal, leading to a more complicated slip system activity, as shown in Fig. 15c. Nevertheless, one can observe that the initial tendency of a positive crystal rotation still prevails (Fig. 14c). Although the same change of the compression axis rotation occurs, due to the high crystal rotations before the contact with the tip is established, this is sufficient only to decelerate the rotation of the crystal, not to reverse it.

6. Conclusions

The main results and conclusions are:

- A physically based constitutive crystal plasticity finite element analysis reveals better agreement with the nanoindentation experiments than a phenomenological viscoplastic material model.
- The complex rotation pattern induced during conical indentation which is characterized by several rotation zones is well predicted when using a physically based constitutive crystal plasticity finite element model. While the crystal rotates in a certain direction in the zone near the indenter axis, the neighboring zone shows the opposite rotation.
- The change of the crystal rotation directions can be explained by the different active slip systems due to the geometry of the indenter causing a gradual change in the loading axis during indentation.
- Although the model succeeded in predicting the pile-up out-of-plane pattern and the rotation pattern under the indent, it slightly overestimates the crystal rotations.
- For the small deformation scales discussed here there might be an effect of the free surfaces created by the FIB technique. Further experimental study in that direction needs to be done in order to estimate the deviation in the measurements with respect to the material condition without milling.

References

[1] Larson BC; personal communication.
[2] McLaughlin KK, Stelmashenko NA, Lloyd SJ, Vandeperre LJ, Clegg WJ. Mater Res Soc Symp Proc 2005;841:3–8.
[3] Lloyd SJ, Castellero A, Giuliani F, Long Y, McLaughlin KK, Molina-Aldareguia JM, Stelmashenko NA, Vandeperre LJ, Clegg WJ. Proc Roy Soc A 2005;461:2521–43.
[4] Zaafarani N, Raabe D, Singh RN, Roters F, Zaefferer S. Acta Mater 2006;54:1863–76.
[5] Brown LM. Mat Sci Forum 2007;550:105–17.
[6] Bouvier S, Needleman A. Modell Simul Sci Eng 2006;14:1105–25.
[7] Kysar JW; http://www.sem.org/NM-kysar.pdf.
[8] Kiener D, Pippan R, Motz C, Kreuzer H. Acta Mater 2006;54:2801–11.
[9] Ma A, Roters F. Acta Mater 2004;52:3603–12.

[10] Ma A, Roters F, Raabe D. Acta Mater 2006;54:2169–79.
[11] Wang Y, Raabe D, Klüber C, Roters F. Acta Mater 2004;52:2229–38.
[12] Liu Y, Wang B, Yoshino M, Roy S, Lu H, Komanduri R. J Mech Phys Solid 2005;53:2718–41.
[13] Casals O, Ocenasek J, Alcala J. Acta Mater 2007;55:55–68.
[14] Zaefferer S, Kuo JC, Zhao Z, Winning M, Raabe D. Acta Mater 2003;51:4719–35.
[15] Ma A, Roters F, Raabe D. Acta Mater 2006;54:2181–94.
[16] Raabe D, Sachtleber M, Zhao Z, Roters F, Zaefferer S. Acta Mater 2001;49:3433–41.
[17] Asaro RJ, Needleman A. Acta Metall 1985;33:923–53.
[18] Wu TY, Bassani JL. Proc Roy Soc A 1991;435:21–41.
[19] Kocks UF. ASME J Eng Mater Tech 1976;98:76–83.
[20] Estrin Y, Mecking H. Acta Metall 1984;32:57–70.
[21] Mughrabi H. Mat Sci Eng 1987;85:15–31.
[22] Zehetbauer M. Acta Metall et Mat 1993;41:589–99.
[23] Estrin Y, Tóth LS, Molinari A, Bréchet Y. Acta Mater 1998;46:5509–22.
[24] Roters F. Realisierung eines Mehrebenenkonzeptes in der Plastizitätsmodellierung. 1999 Ph.D Thesis, RWTH Aachen [in German].
[25] Roters F, Raabe D, Gottstein G. Acta Mater 2000;48:4181–9.
[26] Arsenlis A, Parks DM. J Mech Phys Solid 2002;50:1979–2009.
[27] Granato AV, Lücke K, Schlipf J, Teutonico L. J Appl Phys 1964:2732–45.
[28] MSC. MARC user's manual 2005, User Subroutines and Special Routines, vol. D.
[29] Konrad J, Zaefferer S, Raabe D. Acta Mater 2006;54:1369–80.
[30] Hosford WF. The mechanics of crystals and textured polycrystals. Oxford: Oxford University Press; 1993.